





## Article

# Aggregation-Induced Ignition of Near-Infrared Phosphorescence of Non-Symmetric [Pt(C<sup>N</sup>\*N<sup>^</sup>C<sup>^</sup>)] Complex in Poly(caprolactone)-based Block Copolymer Micelles: Evaluating the Alternative Design of Near-Infrared Oxygen Biosensors

Nina A. Zharskaia <sup>1</sup>, Anastasia I. Solomatina <sup>1</sup>, Yu-Chan Liao <sup>2</sup>, Ekaterina E. Galenko <sup>1</sup>, Alexander F. Khlebnikov <sup>1</sup>, Pi-Tai Chou <sup>2,\*</sup>, Pavel S. Chelushkin <sup>1,\*</sup> and Sergey P. Tunik <sup>1</sup>

<sup>1</sup> Institute of Chemistry, St. Petersburg State University, Universitetskii Av., 26, 198504 St. Petersburg, Russia

<sup>2</sup> Department of Chemistry, National Taiwan University, No. 1, Sec. 4, Roosevelt Rd., Taipei 10617, Taiwan

\* Correspondence: chop@ntu.edu.tw (P.-T.C.); p.chelushkin@spbu.ru (P.S.C.)

**Abstract:** In the present work, we described the preparation and characterization of the micelles based on amphiphilic poly( $\epsilon$ -caprolactone-*block*-ethylene glycol) block copolymer (**PCL-*b*-PEG**) loaded with non-symmetric [Pt(C<sup>N</sup>\*N<sup>^</sup>C<sup>^</sup>)] complex (**Pt1**) (where C<sup>N</sup>\*N<sup>^</sup>C<sup>^</sup>: 6-(phenyl(6-(thiophene-2-yl)pyridin-2-yl)amino)-2-(thiophene-2-yl)nicotinate). The obtained nanospecies displayed the ignition of near-infrared (NIR) phosphorescence upon an increase in the content of the platinum complexes in the micelles, which acted as the major emission component at 12 wt.% of **Pt1**. Emergence of the NIR band at 780 nm was also accompanied by a 3-fold growth of the quantum yield and an increase in the two-photon absorption cross-section that reached the value of 450 GM. Both effects are believed to be the result of progressive platinum complex aggregation inside hydrophobic poly(caprolactone) cores of block copolymer micelles, which has been ascribed to aggregation induced emission (AIE). The resulting phosphorescent (**Pt1@PCL-*b*-PEG**) micelles demonstrated pronounced sensitivity towards molecular oxygen, the key intracellular bioanalyte. The detailed photophysical analysis of the AIE phenomena revealed that the NIR emission most probably occurred due to the excimeric excited state of the <sup>3</sup>MMLCT character. Evaluation of the **Pt1@PCL-*b*-PEG** efficacy as a lifetime intracellular oxygen biosensor carried out in CHO-K1 live cells demonstrated the linear response of the probe emission lifetime towards this analyte accompanied by a pronounced influence of serum albumin on the lifetime response. Nevertheless, **Pt1@PCL-*b*-PEG** can serve as a semi-quantitative lifetime oxygen nanosensor. The key result of this study consists of the demonstration of an alternative approach for the preparation of NIR biosensors by taking advantage of in situ generation of NIR emission due to the nanoconfined aggregation of Pt (II) complexes inside the micellar nanocarriers.

**Keywords:** Pt(II) complexes; aggregation-induced emission; polymer micelles; phosphorescence lifetime imaging; oxygen biosensors



**Citation:** Zharskaia, N.A.; Solomatina, A.I.; Liao, Y.-C.; Galenko, E.E.; Khlebnikov, A.F.; Chou, P.-T.; Chelushkin, P.S.; Tunik, S.P. Aggregation-Induced Ignition of Near-Infrared Phosphorescence of Non-Symmetric [Pt(C<sup>N</sup>\*N<sup>^</sup>C<sup>^</sup>)] Complex in Poly(caprolactone)-based Block Copolymer Micelles: Evaluating the Alternative Design of Near-Infrared Oxygen Biosensors. *Biosensors* **2022**, *12*, 695. <https://doi.org/10.3390/bios12090695>

Received: 21 July 2022

Accepted: 24 August 2022

Published: 28 August 2022

**Publisher's Note:** MDPI stays neutral with regard to jurisdictional claims in published maps and institutional affiliations.



**Copyright:** © 2022 by the authors. Licensee MDPI, Basel, Switzerland. This article is an open access article distributed under the terms and conditions of the Creative Commons Attribution (CC BY) license (<https://creativecommons.org/licenses/by/4.0/>).

## 1. Introduction

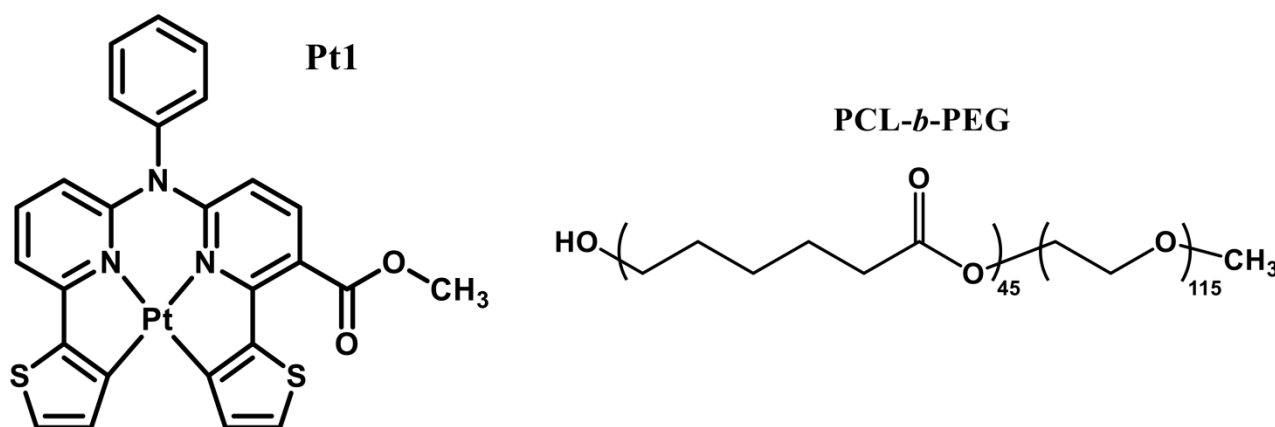
Since the coining of the term “Aggregation-Induced Emission (AIE)” by B. Z. Tang’s group in 2001 [1], various aggregation-induced [2–4] or aggregation-enhanced [5] photophysical phenomena have been described. Such an intense focus on AIE and related phenomena stems from realizing the potential benefits of implementing AIE-based emitters (AIEgens) in applications utilizing high emitter concentrations, such as OLED technology [1], organelle-specific imaging and sensing [6], as well as photodynamic therapy [7]. The major advantage of these emitters is that contrary to conventional emitters that quench upon concentrating, AIEgens ignite or enhance their luminescence, two-photon emission, singlet oxygen production, etc. [2–4].

Because the very essence of AIE lies in the rigidification of the emitters' microenvironment that restricts intramolecular motions and thus suppresses the rotovibrational relaxation of excited states [2–4], one can expect that organometallic compounds, in line with “classical” organic AIEgens, are also prone to exert AIE and related phenomena. Indeed, recent reports reviewed in [8] demonstrated that various (iridium(III) [9,10], ruthenium(II) [11,12], rhenium(I) [13–15], gold(I) [16], etc.) organometallic complexes also demonstrate AIE or related photophysical (e.g., increase in two-photon emission cross-sections [10]) and photochemical (e.g., enhancement of singlet oxygen generation [9,10]) behavior. In this context, square planar Pt(II) complexes are among the ‘brightest’ examples demonstrating AIE and related phenomena [5,17–20].

Organometallic AIEgens based on Pt(II) complexes are unique objects because they combine high sensitivity to oxygen (which naturally stems from the triplet nature of their excited states effectively quenched by triplet molecular oxygen) with a pronounced bathochromic shift of luminescence due to the emergence of metal–metal-to-ligand charge-transfer (<sup>3</sup>MMLCT) states [5,17–20] arising as a result of intermolecular Pt . . . Pt interaction. The most important practical result of this combination of properties is that such AIEgens can provide a new strategy for the design of NIR phosphorescent oxygen nanosensors. Indeed, despite the impressive progress in the field of phosphorescent O<sub>2</sub> sensors such as the development of NIR O<sub>2</sub> sensors based on single molecules protected by oligo(ethylene glycol) [21,22], dendronized poly(ethylene glycol) (Oxyphor 2P [23]), embedded in polymer nanoparticles (NanO<sub>2</sub>-IR [24]), or developing macroscopic sensors for in vivo [25] and inside 3D cell cultures [26], the main paradigm of their design (i.e., using increasingly sophisticated organometallic complexes that possess NIR emission in a monomeric state [27]) is still a challenging synthetic task. Alternative approaches for the generation of NIR phosphorescence are required, where shifting the phosphorescence emission to NIR due to AIE could provide the desired opportunity.

In view of the possible practical applications of organometallic AIEgens as oxygen biosensors, their dispersion stability and compact packing are of significant importance. Generally, AIE can be spatially restricted to small (down to nanometer scale) volumes, which seems to be quite useful in numerous applications [7]. In particular, such a nanoconfinement of AIE provides the possibility for the controlled design of nanoparticle-based oxygen biosensors, as was reported recently for the sensor prototype based on symmetrical [Pt(C<sup>∧</sup>N<sup>\*</sup>N<sup>∧</sup>C)] complexes embedded into aminated polystyrene nanoparticles that demonstrated aggregation-enhanced dual emission in the green and deep red areas of the visible spectrum [5]. Notably, the dispersion stability of the polystyrene nanoparticles used in the above study was based on electrostatic repulsions of amino groups; this type of stabilization is not sufficient in aqueous saline media due to electrostatic screening by low molecular weight salts [28].

In our own research, we recently developed a series of Pt(II) complexes with non-symmetric C<sup>∧</sup>N<sup>\*</sup>N<sup>∧</sup>C' ligands and found that one of these [Pt(C<sup>∧</sup>N<sup>\*</sup>N<sup>∧</sup>C')] complexes (here and below referred to as **Pt1**; Scheme 1) displays an orange emission in its monomeric form but demonstrates the appearance of AIE in the near-infrared (NIR) region [29]. Taking into account the fact that the NIR emission fits well into the so-called “biological transparency window” (a region from 650 to 900 nm where light penetrates into tissues much deeper compared to radiation of visible spectral interval [30]), we decided to evaluate the performance of this complex in oxygen sensing. To implement the idea of AIE nanoconfinement, we embedded the **Pt1** complex into block copolymer micelles prepared from poly( $\epsilon$ -caprolactone-*block*-ethylene glycol) (**PCL-*b*-PEG**; Scheme 1). This amphiphilic diblock copolymer forms ‘core–shell’ type micelles, which proved to be more promising nanocarriers compared to ‘plain’ polymer nanoparticles and latexes due to their improved stability in saline aqueous dispersions [31]. The resulting **Pt1@PCL-*b*-PEG** nanosensor demonstrated prominent AIE-based NIR emission in combination with improved dispersion stability and an appreciable lifetime sensitivity to oxygen.



**Scheme 1.** Chemical structures of complex **Pt1** and **PCL-*b*-PEG** block copolymer used in the study.

## 2. Materials and Methods

### 2.1. General Comments

All the basic laboratory procedures and measurement protocols are described in detail in Part 1 of the Supplementary Materials. Additionally, experiments such as the estimation of micelles' loading by **Pt1** with UV/Vis absorption spectroscopy, dynamic light scattering and photophysical experiments, as well as cell culture maintenance and a cell viability (MTT [32]) assay were performed using the protocols developed in our previous publication on phosphorescent micelles [31] with slight modifications. Hypoxia in cells was induced by blowing the nitrogen-air mixture at preset volume ratio above the cell monolayer for ca. 30 min [21,33]. The exact protocols used in the present study can also be found in Part 1 of the Supplementary Materials.

### 2.2. Handling of **PCL-*b*-PEG** Block Copolymers and Preparation of Block Copolymer Micelles

The 2 samples of **PCL-*b*-PEG** used in the study were both purchased from "Sigma-Aldrich", St. Louis, MO, USA (Product # 570303). A summary of the characterization of both samples by <sup>1</sup>H NMR and GPC is presented in Table S1 and Figure S1.

Sample #1 was identical to that used in our previous work [31]. In the case of this sample, the protocol reported earlier [31] facilitated the reproducible preparation of almost transparent micellar dispersions without signs of precipitation for both 'empty' **PCL-*b*-PEG** micelles and those loaded by **Pt1** (**Pt1@PCL-*b*-PEG**), so we used this protocol for all the preparations based on sample #1.

Sample #2 was new; in the case of this sample, using of the same protocol [31] resulted in the formation of turbid micellar dispersions that yielded precipitates during preparative centrifugation for at least 15 min at 15,000 rpm. Consequently, before its further use in micelle preparation, sample #2 was 'purified' by performing the following cycles: first, micelles were prepared by the protocol reported earlier [31]; then, the dispersions were separated from the sedimentally unstable fraction by performing preparative centrifugation followed by freeze drying of the supernatant. The resulting lyophilizate was used as a starting material for the next cycle. After three cycles described above, the 'purified' version of **PCL-*b*-PEG** sample #2 was obtained with an overall yield of 80%. This sample formed almost transparent micellar dispersions.

In the case of the 'purified' version of **PCL-*b*-PEG** sample #2, use of the preparation protocol described earlier [31] for the formation of 'loaded' **Pt1@PCL-*b*-PEG** micelles led occasionally to parallel precipitation of **Pt1**, so in this case we used a slightly modified preparation protocol featuring a faster and more uniform addition of water via the syringe operated by a speed-adjustable stepping motor and an elevated temperature of the reaction mixture from ambient (ca. 25 °C) to 40 °C. The modified protocol consisted of the separate dissolving of both starting components (block copolymers and complex **Pt1**) in DMF to obtain stock solutions of 30 mg/mL for **PCL-*b*-PEG** of 5 mg/mL for **Pt1**, their subsequent

mixing at appropriate weight proportions resulting in the **Pt1**:block copolymer mixtures with 0 ('empty' micelles), 2, 6, 9, or 12 wt.% of the complex **Pt1** at 40 °C followed by the addition of 3 volumes of type 1 water under vigorous stirring (1200 rpm) to form the micelles. The flow rate of water was adjusted to accomplish the addition of water within 15 min or less (typically, this required the flow rate of 0.2 mL/min) to avoid **Pt1** precipitation. Water was added via a 10 mL sterile disposable syringe operated by a speed-adjustable stepping motor (model: YH42BYGH60-401A, "Cnyoho", China) to provide a steady flow of the liquid. The dispersions were then purified from DMF by performing dialysis using "Spectra/Por®4" dialysis tubes ("Scienova", Germany) with a molecular weight cut-off of 12–14 kDa against type 1 water (5–7 water changes). The obtained micelle dispersions were transferred into pre-weighed 12 mL vials to evaluate mass concentration and stored in a fridge in the dark at 4 °C. Measured mass concentrations of the final dispersion were obtained by the weighting of lyophilizates obtained by performing freeze-drying of pre-weighed aliquots of the dispersions. Measured and evaluated concentrations of the dispersion agreed well within the experimental error (less than 12%).

### 2.3. Measurements of Two-Photon Properties

The two-photon absorption (TPA) cross section of **Pt1@PCL-b-PEG** at 800 nm was measured by performing an open aperture Z-scan experiment, where a mode-locked Ti: sapphire laser (Tsunami, Spectra Physics) producing single Gaussian pulse (800 nm) was coupled to a regenerative amplifier to generate an approx. 180 fs and 1 mW pulse (760–840 nm, 1 kHz, Spitfire, Spectra Physics) as the excitation source. The pulse energy, after appropriate attenuation, was then reduced to ~1.2–1.8 µJ. After passing through an  $f = 7.5$  cm lens, the laser beam was focused and passed through a 1.00 mm cell with solution ( $4 \times 10^{-4}$ – $1 \times 10^{-3}$  M), and the beam radius at the focal position was 0.1 cm. When the sample cell changed its position along the beam direction (z-axis), the transmitted laser beam from the sample cell was detected by a photodiode (PD-9, Ophir). The TPA-induced decrease in transmittance,  $T(z)$ , can be expressed as Equations (1) and (2), and the TPA coefficient ( $\beta$ ) can be obtained from experimental data by fitting Z-scan curves to Equations (1) and (2).

$$T(z) = \sum_0^{\infty} \frac{(-q)^n}{(n+1)^{3/2}} \quad (1)$$

$$q = \frac{\beta I_0 L}{1 + \frac{z^2}{z_0^2}}, \quad (2)$$

where  $n$  is an integer number from 0 to  $\infty$  and is truncated at  $n = 30$ ,  $L$  is the sample length and  $I_0$  is the input intensity.  $z_0$  is the diffraction length of the incident beam (Rayleigh range). After obtaining the TPA coefficient ( $\beta$ ; Equation (3)), the TPA cross section ( $\sigma_{\text{TPA}}$ ) can be deduced by using Equation (3), where  $N_A$  is the Avogadro number,  $d$  is the concentration,  $h$  is the Planck constant, and  $\nu$  is the frequency of the incident beam. The error of TPA measurement when utilizing the Z-scan method was in the range of <5% after five replicas.

$$\beta = \frac{\sigma_{\text{TPA}} N_A d \times 10^{-3}}{h\nu} \quad (3)$$

### 2.4. Confocal Microscopy and PLIM

Living cells were imaged by using a confocal inverted Nikon Eclipse Ti2 microscope (Nikon Corporation, Tokyo, Japan) with 60× oil immersion and 40× water immersion objectives. The images were recorded using the following standard settings: excitation at 405 nm and emission at 663–738 nm. Differential interference contrast (DIC) images were also recorded in addition to fluorescence microphotographs. Phosphorescence lifetime imaging microscopy (PLIM) of cells was carried out using the TCSPC DSC-120 module (Becker & Hickl GmbH, Berlin, Germany) integrated into the confocal device. A picosecond laser (405 nm) was used as an excitation source. The phosphorescence of the probe

was recorded in two channels using a (1) 630/75 nm band pass filter and pinhole of 0.5, (2) 720/60 nm band pass filter and pinhole of 1.0. In normoxic conditions, the following PLIM acquisition parameters were used: frame time 20.82 s, pixel dwell time 78.90  $\mu$ s, points number 1024, time per point 75.00 ns, time range of PLIM recording 76.80  $\mu$ s, total acquisition time 100–130 s, and image resolution 512  $\times$  512 pixels. In hypoxic conditions, the parameters were as follows: frame time 41.97 s, pixel dwell time 159.6  $\mu$ s, points number 1024, time per point 150.00 ns, time range of PLIM recording 153.60  $\mu$ s, total acquisition time 100–150 s, and image resolution 512  $\times$  512 pixels. Oil immersion 60 $\times$  objective with zoom 5.33 provided a scan area of ca. 0.05 mm  $\times$  0.05 mm. Water immersion 40 $\times$  objective with zoom 5.33 provided a scan area of ca. 0.08 mm  $\times$  0.08 mm. Phosphorescence lifetime distributions were calculated using SPCImage 8.1 software (Becker & Hickl GmbH, Berlin, Germany). The decay curves were fit as triexponential decay with an average goodness of fit of  $0.8 \leq \chi^2 \leq 1.1$ . The average number of photons under the decay curve were  $\geq 5000$  at binning of 7–8.

### 3. Results

#### 3.1. Preparation and Structural Characterization of Phosphorescent Micelles

Two samples of **PCL-*b*-PEG** block copolymer were used in the study. Sample #1 was identical to that used in our previous work [31]. Its [PEG]:[PCL] ratio calculated from  $^1\text{H}$  NMR spectra (Figure S1) was 4.4:1.0, which exceeded the corresponding value expected from  $M_n$  values of blocks ( $M_n(\text{PEG}) = M_n(\text{PCL}) = 5000$ ; [PEG]:[PCL] = 2.6:1.0) provided by the manufacturer (Table S1). The average molecular weight ( $M_w$ ) and dispersity ( $\mathcal{D}$ ) of this sample also slightly exceeded the corresponding values provided by the manufacturer, but were in reasonable agreement with these data (Table S1). ‘Empty’ micelles from this sample were prepared by performing the protocol reported earlier [31]; these micellar dispersions were almost transparent and lacked any signs of precipitation; the corresponding hydrodynamic radii ( $R_h$ ) distribution obtained by DLS was reported to be almost unimodal with trace amounts of larger (60–200 nm) particles while the average  $R_h$  value was reported to be 17.7 nm [31].

Sample #2 has not been reported previously. The  $^1\text{H}$  NMR spectrum of the starting polymer (“Sigma-Aldrich”, St. Louis, MO, USA; Product # 570303) was almost identical to that of sample #1 (Figure S1) but displayed a slightly lower [PEG]:[PCL] ratio (3.8:1.0) that indicates its lower hydrophilicity (i.e., lower PEG content) compared to sample #1. GPC revealed that sample #2 had a lower  $M_w$  ( $M_w(\text{sample } \#2) = 10,800$  compared to  $M_w(\text{sample } \#1) = 15,000$ ; Table S1) and higher dispersity ( $\mathcal{D}(\text{sample } \#2) = 1.41$  compared to  $\mathcal{D}(\text{sample } \#1) = 1.33$ ; Table S1). Most probably, the lower [PEG]:[PCL] ratio (i.e., lower hydrophilicity) and higher dispersity were the major reasons for sample #2 to form substantially turbid micellar dispersions, which eventually yielded precipitates. Nevertheless, three repetitive cycles of precipitate separation (micelle preparation/precipitate separation by preparative centrifugation/freeze drying of the supernatant; see Section 2.2. in Materials and Methods for more details) allowed us to obtain the ‘purified’ version of **PCL-*b*-PEG** sample #2 with lower  $\mathcal{D} = 1.31$  and [PEG]:[PCL] = 4.5:1.0 (both these parameters of ‘purified’ sample #2 appeared to be very close to those of sample #1; Table S1). This ‘purified’ sample #2 reproducibly formed almost transparent micellar dispersions. The corresponding  $R_h$  distribution of micelles based on the ‘purified’ sample #2 obtained by DLS was almost unimodal with similar trace amounts of larger (100–200 nm) particles and had average  $R_h$  values of  $22 \pm 2$  nm (Figure 1A). Because  $M_w$ ,  $\mathcal{D}$ ,  $R_h$  distributions, and average  $R_h$  values of the sample #1 and the ‘purified’ sample #2 were essentially similar, both **PCL-*b*-PEG** samples were used in the study interchangeably.

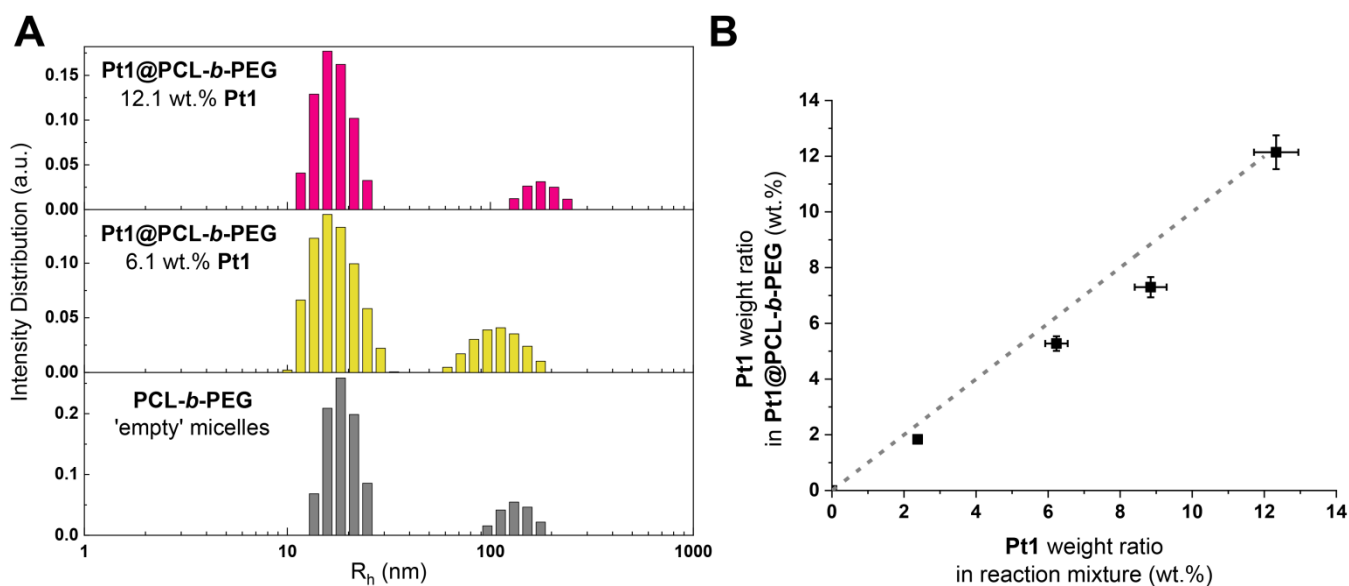


**Figure 1.** (A). Intensity weighted  $R_h$  distributions of ‘empty’ PCL-*b*-PEG (grey) and ‘loaded’ Pt1@PCL-*b*-PEG (6.1 (yellow) and 12.1 (red) wt.% Pt1) micelles measured at 90 °C = 0.25 mg/mL. (B). Dependence of Pt1 weight ratio in Pt1@PCL-*b*-PEG block copolymer micelles as a function of Pt1 weight ratio in reaction mixture (black squares). Dashed line denotes theoretical dependence corresponding to 100% loading efficiency.

Loading of Pt1 into PCL-*b*-PEG micelles (i.e., formation of Pt1@PCL-*b*-PEG micelles) required a slight modification of the preparation protocol used previously [31] due to the pronounced tendency of Pt1 to precipitate in the water:DMF mixtures even in the presence of block copolymer micelles. Nevertheless, the faster (accomplished in less than 15 min) and steadier addition of water (via the syringe operated by speed-adjustable stepping motor) into the reaction mixture at a slightly elevated temperature (40 °C) made possible the successful preparation of Pt1@PCL-*b*-PEG micelles. The resulting content of Pt1 in the micelles was only slightly lower than that in the starting reaction mixture (Figure 1B). Investigation of Pt1@PCL-*b*-PEG micelles by DLS revealed that their  $R_h$  distributions were almost unimodal (Figure 1A) with a minor peak of larger (of approx. 80–200 nm) particles and closely resembled the  $R_h$  distribution of ‘empty’ micelles. The average  $R_h$  values of Pt1@PCL-*b*-PEG micelles were  $19 \pm 2$  and  $18 \pm 2$  nm at 6.1 wt.% and 12.1 wt.% of Pt1, respectively. The ‘empty’ and ‘loaded’ micelles prepared via the modified protocol were stable during preparative centrifugation for 15 min at 20,000 rpm without any precipitation. Additionally, no phase separation or precipitation was observed at concentrations of up to 3 mg/mL, the upper concentration limit in stock solutions, as well as during dilution or storage at 4 °C for at least two weeks. Similar stability was observed in PBS solutions.

### 3.2. Photophysical Characterization of Phosphorescent Micelles

Photophysical characterization of Pt1@PCL-*b*-PEG started with the measurements of absorption, excitation and luminescence spectra of Pt1@PCL-*b*-PEG samples with Pt1 loading ranging from 1.8 to 12.1 wt.%. Figure 2A,B demonstrate that the variation of the Pt1 content in micelles does not affect the absorption and excitation spectra (see also Figure S3 for more detailed representations of excitation spectra recorded at 605 and 780 nm, respectively). On the contrary, the corresponding luminescence spectra change drastically; in addition to the structured emission band of non-aggregated Pt1 with the major peak at 605 nm, the increase in Pt1 loading led to the appearance of a new emission band in the NIR range (Figure 2C). Moreover, the overall emission intensity increased with increased loading of Pt1 into the micelles (Figure S4). Deconvolution of the spectral pattern (subtraction of monomolecular Pt1 spectra in THF from those of Pt1@PCL-*b*-PEG) revealed that the profile of this NIR band does not depend on Pt1 content and appears as a broad

symmetrical band centered at ca. 790 nm with a half-width of ca. 180 nm (Figure 2D). It is also worth noting that the increase in the **Pt1** content resulted in a strong increase in the relative intensity of the NIR band and became dominant starting from approx. 8 wt.% of **Pt1** (Figure 2C). The quantum yield values measured in aerated aqueous dispersions of **Pt1**@**PCL-*b*-PEG** increased from 2% for 2.5 wt.% of **Pt1** loading to 6% for 12.4 wt.% of **Pt1** loading.

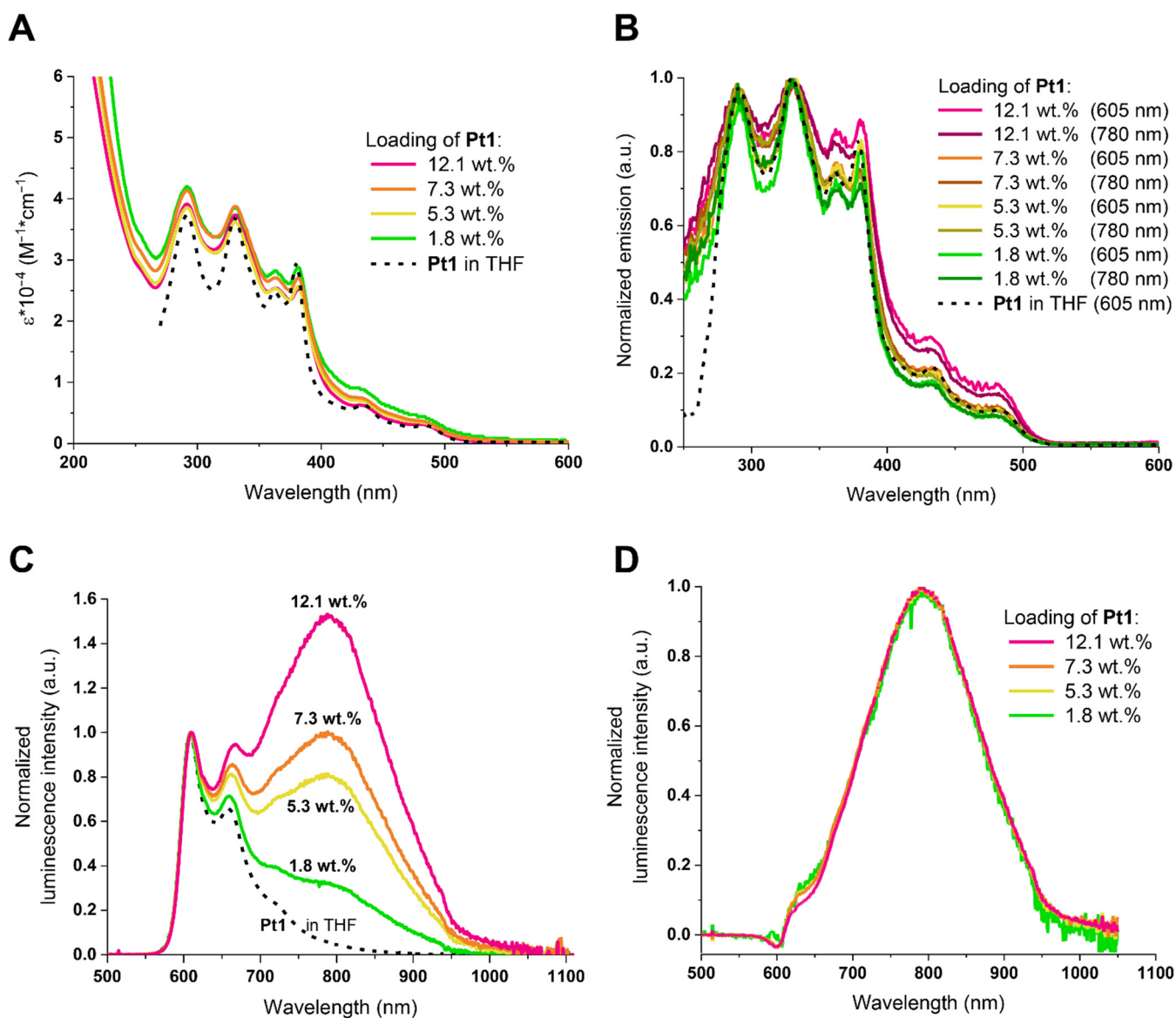


**Figure 2.** Photophysical properties of **Pt1**@**PCL-*b*-PEG** micellar dispersions in water. (A). Absorption spectra. (B). Normalized excitation spectra detected at 605 and 780 nm. (C). Normalized emission spectra. Excitation at 365 nm. Dashed line represents emission spectrum of **Pt1** in THF. (D). Normalized differential spectra of **Pt1** NIR emission band in the **PCL-*b*-PEG** micelles.

To understand the nature of the excited state, the nanosecond time-resolved measurement was performed by using TCSPC. As shown in Figure S5, a corresponding decay and rise of about 19.54 ns was detected upon monitoring the dual emission at 605 nm and 790 nm, respectively, for **Pt1**@**PCL-*b*-PEG** (2.3 wt.% of **Pt1**) in the aerated water. Therefore, the dual emission possesses a precursor–successor type of relationship whereby the NIR 790 nm emission (successor) originates from the relaxation of the 605 nm monomer emission (precursor). This viewpoint is also supported by the identical excitation spectrum between

two monitored emission regions, e.g., 605 and 790 nm. Together with the concentration-dependent emission spectra, the 790 nm NIR emission was most plausibly assigned to the excimer emission of **Pt1** aggregates.

In our recent publication [29], two-photon absorption ( $\sigma_{\text{TPA}}$ ) and emission ( $\sigma_{\text{TPE}}$ ) cross-sections of **Pt1** in organic solvents were measured by a comparative method to produce the values of 20 and 10 GM, respectively. Since the observed aggregation can also enhance non-linear optical properties of **Pt1**, we measured the  $\sigma_{\text{TPA}}$  for **Pt1@PCL-*b*-PEG** micelles, too. As a result, the two-photon absorption cross section ( $\sigma_{\text{TPA}}$ ) of **Pt1@PCL-*b*-PEG** (2.3 wt.% of **Pt1**) deduced by performing the Z-scan method was  $450 \pm 22$  GM (800 nm) (see Figure S6). This value significantly improved compared to the **Pt1** monomer ( $130 \pm 10$  GM at 800 nm) estimated by the same method.

Lifetime measurements for the **Pt1@PCL-*b*-PEG** micelles loaded with 2.3 and 12.1 wt.% of the platinum complex were also carried out in different media and at different partial pressures of oxygen, see Figure 3, Figures S7 and S8; Table 1, Tables S2 and S3. A detailed investigation of the emission decay curves collected at different detection wavelengths (605, 665, 725 nm, Table S2) indicated that in the case of data acquisition with reliable statistics ( $10^4$  photon counts) the biexponential fitting provides the following results: the lifetime of the dominant exponent ( $\tau_{\text{major}}$ ) remains unchanged within the experimental uncertainty ( $\tau_{\text{major}} = 0.71 \pm 0.02$  s for **Pt1@PCL-*b*-PEG** loaded by 12.1 wt.% of **Pt1** in aerated water dispersion at 37.6 °C), and its contribution in the decay varies from 92 to 95% (Table S2). These observations indicate that for the **Pt1@PCL-*b*-PEG** samples containing 12.1 wt.% of the complex (1) the emission decay curves in water and PBS (Figures S7 and S8) may be successfully fitted with the monoexponential function (Table 1 and Table S2) and (2) lifetime measurements may be carried out using any of these detection wavelengths due to the major contribution of the NIR emission band to the decay independent of the wavelength choice. Lifetimes data at different  $\text{O}_2$  partial pressures were used to construct Stern–Volmer plots for **Pt1@PCL-*b*-PEG** dispersions (with **Pt1** loading ranging from 2.3 to 12.1 wt.%) in water and PBS at 37.6 °C (Figure 3A). Lifetime sensitivity to oxygen estimated as the  $\tau_0/\tau_{160}$  ratio (where  $\tau_0$  refers to 0 mmHg  $\text{O}_2$ ,  $\tau_{160}$  to 160 mmHg  $\text{O}_2$ ) varied from 3.0 for the dispersions with 2.3 wt.% of **Pt1** ( $\tau_{160} = 1.30 \pm 0.07$  s;  $\tau_0 = 3.9 \pm 0.2$   $\mu\text{s}$ ) to approx. 1.5 for that with 12.1 wt.% of **Pt1** ( $\tau_{160} = 0.60 \pm 0.03$   $\mu\text{s}$ ;  $\tau_0 = 0.92 \pm 0.05$   $\mu\text{s}$ ), see Figure 3B and Table 1. The corresponding Stern–Volmer plots were linear for all micellar compositions (Figure 3A). Stern–Volmer constants ( $K_{\text{SV}}$ ) display values from  $0.0033 \pm 0.0002$   $\text{mmHg}^{-1}$  (**Pt1** loading: 12.1 wt.%) to  $0.0124 \pm 0.0001$   $\text{mmHg}^{-1}$  (**Pt1** loading: 2.3 wt.%) in Table 1.  $K_{\text{SV}}$  values strongly depend on **Pt1** loading and level off above the compositions of 9 wt.% **Pt1**, whereas quenching constants,  $K_{\text{Q}}$  do not depend on the **Pt1** content and equal to  $0.0034 \pm 0.0002$   $\mu\text{s}^{-1}\text{mmHg}^{-1}$  for all studied micelles (Table 1).

**Table 1.** Summary of time-resolved parameters for **Pt1@PCL-*b*-PEG** with different **Pt1** loadings <sup>a</sup>.

Loading of Pt1	DispersionMedium	$\tau_0, \mu\text{s}$	$\tau_{160}, \mu\text{s}$	$K_{\text{Q}}, \mu\text{s}^{-1} \text{mmHg}^{-1}$	$K_{\text{SV}}, \text{mmHg}^{-1}$
2.3 wt.%	H <sub>2</sub> O	$3.9 \pm 0.2$	$1.30 \pm 0.07$	$0.00320 \pm 0.00002$	$0.0124 \pm 0.0001$
	PBS	$4.1 \pm 0.2$	$1.30 \pm 0.07$	$0.00325 \pm 0.00004$	$0.0132 \pm 0.0003$
6.1 wt.%	H <sub>2</sub> O	$1.38 \pm 0.07$	$0.80 \pm 0.04$	$0.0033 \pm 0.0001$	$0.0046 \pm 0.0002$
	PBS	$1.47 \pm 0.07$	$0.78 \pm 0.04$	$0.0038 \pm 0.0003$	$0.0056 \pm 0.0005$
8.7 wt.%	H <sub>2</sub> O	$1.04 \pm 0.05$	$0.67 \pm 0.03$	$0.0032 \pm 0.0001$	$0.0034 \pm 0.0001$
	H <sub>2</sub> O	$0.92 \pm 0.05$	$0.60 \pm 0.03$	$0.0036 \pm 0.0002$	$0.0033 \pm 0.0002$
12.1 wt.%	H <sub>2</sub> O	$0.92 \pm 0.05$	$0.60 \pm 0.03$	$0.0036 \pm 0.0002$	$0.0033 \pm 0.0002$
	PBS	$0.93 \pm 0.05$	$0.59 \pm 0.03$	$0.0039 \pm 0.0002$	$0.0036 \pm 0.0002$

<sup>a</sup> All the measurements were performed at excitation and detection wavelengths of 355 and 605 nm, correspondingly. All  $\tau$  values were obtained from monoexponential fittings of the decay curves.



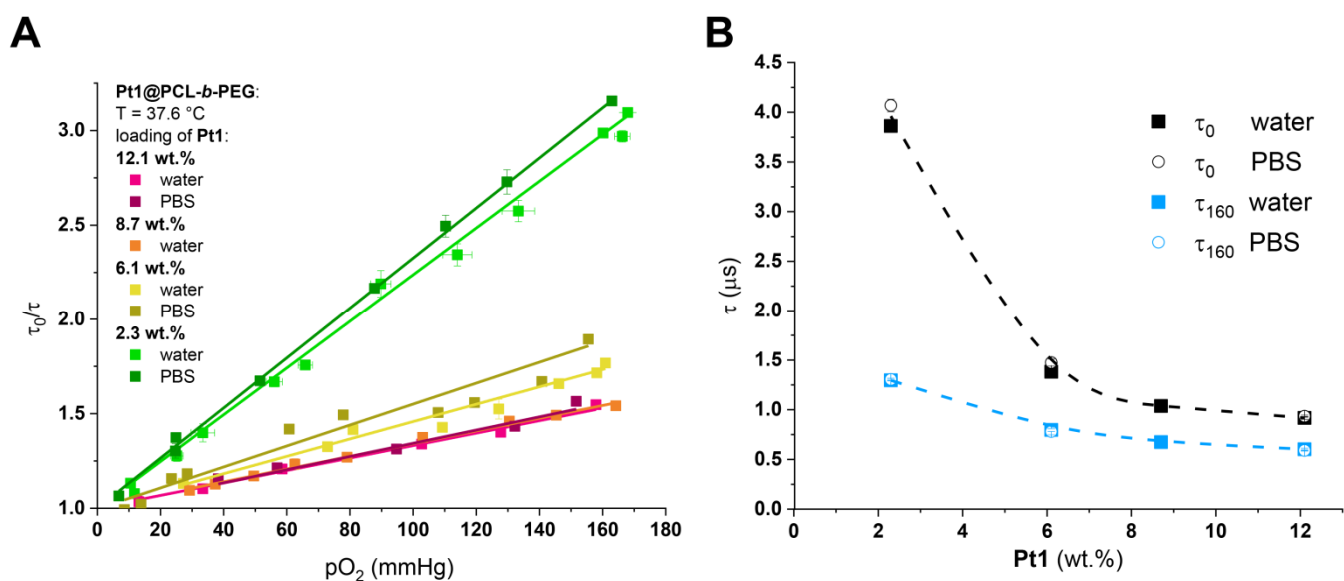


**Figure 3.** (A). Stern–Volmer plots for Pt1@PCL-*b*-PEG of various Pt1 loadings in water and PBS. (B). Dependence of lifetime in fully degassed (extrapolated to 0 mmHg O<sub>2</sub>) and aerated (interpolated to 160 mmHg O<sub>2</sub>) on composition of Pt1@PCL-*b*-PEG in PBS dispersions at 37.6 °C. Lifetime data were acquired at 605 nm,  $\lambda_{exc} = 365$  nm.

We also studied the effects of the other media variables (pH, temperature, ionic strength, presence of H<sub>2</sub>O<sub>2</sub> and bovine serum albumin) as well as the influence of the probe concentration on the lifetimes of aerated dispersions of Pt1@PCL-*b*-PEG (2.3 and 12.1 wt.% of Pt1), see Table 2. Lifetimes of these chromophores did not depend on the probe concentration, pH, ionic strength, and H<sub>2</sub>O<sub>2</sub> (Table 2) but proved to be sensitive to the Pt1 content in the micelles, temperature, and to the presence of bovine serum albumin (BSA). In the case of BSA, the decay curves became non-monoexponential (Table 2), and mean lifetime values were more than 1.5 times higher compared to those in water and PBS.

**Table 2.** Luminescence lifetimes of aerated dispersions of Pt1@PCL-*b*-PEG (2.3 and 12.1 wt.%) at various external conditions.

Dispersion	C, mg/mL	pH	T, °C	2.3 wt.% Pt1		12.1 wt.% Pt1	
				pO <sub>2</sub> , mmHg	$\tau$ , $\mu$ s	pO <sub>2</sub> , mmHg	$\tau$ , $\mu$ s
H <sub>2</sub> O	0.2	n.d.	37.6	160.2 ± 0.4	1.29 ± 0.06	157.9 ± 0.5	0.60 ± 0.03
PBS	0.2	7.2	<b>25.6</b>	161 ± 2	1.82 ± 0.09	149.5 ± 0.7	0.85 ± 0.04
PBS	0.2	7.2	37.6	163.0 ± 0.6	1.29 ± 0.06	152 ± 1	0.60 ± 0.03
PBS	<b>0.4</b>	7.2	37.6	155.5 ± 0.6	1.34 ± 0.06	151.6 ± 0.8	0.60 ± 0.03
PBS	0.2	<b>8.1</b>	37.6	162.1 ± 0.2	1.26 ± 0.06	153.9 ± 0.4	0.63 ± 0.05
PBS	0.2	<b>6.6</b>	37.6	166 ± 2	1.28 ± 0.06	157.7 ± 0.8	0.60 ± 0.04
PBS	0.2	<b>5.8</b>	37.6	170 ± 2	1.26 ± 0.06	155.0 ± 0.7	0.61 ± 0.05
PBS + H <sub>2</sub> O <sub>2</sub> (100 nM)	0.2	7.2	37.6	158 ± 1	1.31 ± 0.06	not determined	
PBS + BSA	0.2	7.2	37.6	160 ± 2	1.88 ± 0.09 <sup>a</sup>	154.2 ± 0.4	1.14 ± 0.06 <sup>b</sup>

Bold numbers denote the specific parameters that were varied in each particular experiment. <sup>a</sup> Decay curves were fitted by biexponential decay with  $\tau = (A_1\tau_1^2 + A_2\tau_2^2)/(A_1\tau_1 + A_2\tau_2)$ . <sup>b</sup> Decay curves were fitted by triexponential decay with  $\tau = (A_1\tau_1^2 + A_2\tau_2^2 + A_3\tau_3^2)/(A_1\tau_1 + A_2\tau_2 + A_3\tau_3)$ .

Further analysis of lifetimes was performed in complicated physiological media, namely, 85 vol.% fetal bovine serum, FBS; 85 vol.% calf serum, CS; 42.5 mg/mL BSA (this concentration is an equivalent of protein concentration in 85 vol.% serum). In these cases,

lifetimes depended strongly on media composition and grew up to 4–5  $\mu\text{s}$  in aerated and 8–10  $\mu\text{s}$  in deaerated conditions with rather high media-to-media variations (Table S3). Notably, the relative contribution of the NIR band substantially decreased (Figure S9) in the FBS and BSA solution of the equivalent concentration (42.5 mg/mL) while smaller concentrations of BSA (0.25 mg/mL) and variations in ionic strength (PBS vs. water) did not influence the luminescence spectrum of Pt1@PCL-*b*-PEG (Figure S9).

The biologically relevant calibration of Pt1@PCL-*b*-PEG oxygen sensors vs. oxygen partial pressure was performed using Pt1@PCL-*b*-PEG dispersions with 12.1 wt.% Pt1 in 85 vol.% fetal bovine serum (FBS) at 37 °C and a PLIM setup. The sensor signal was collected using two channels, namely red (595–665 nm) and NIR (690–750 nm). The decay curves in this case were essentially non-monoexponential (Figure S8) and treatment of all the decay curves was performed by implementing triexponential fitting. The resulting Stern–Volmer plots collected from both channels were linear but did not overlay each other, see Figure 4A. In addition, the mean lifetimes of the same probe measured in cuvette in different media at a detection wavelength of 605 nm were overlaid for comparison. These data demonstrate that mean lifetime values measured using the PLIM setup were similar to their counterparts measured in cuvette. The resulting Stern–Volmer plots were linear and provided  $\tau_0 = 9.7 \pm 0.5 \mu\text{s}$  and  $K_{SV} = 0.0093 \pm 0.0009 \text{ mmHg}^{-1}$  for the case of the red channel and  $\tau_0 = 5.9 \pm 0.3 \mu\text{s}$  and  $K_{SV} = 0.0090 \pm 0.0006 \text{ mmHg}^{-1}$  for the case of the NIR channel.

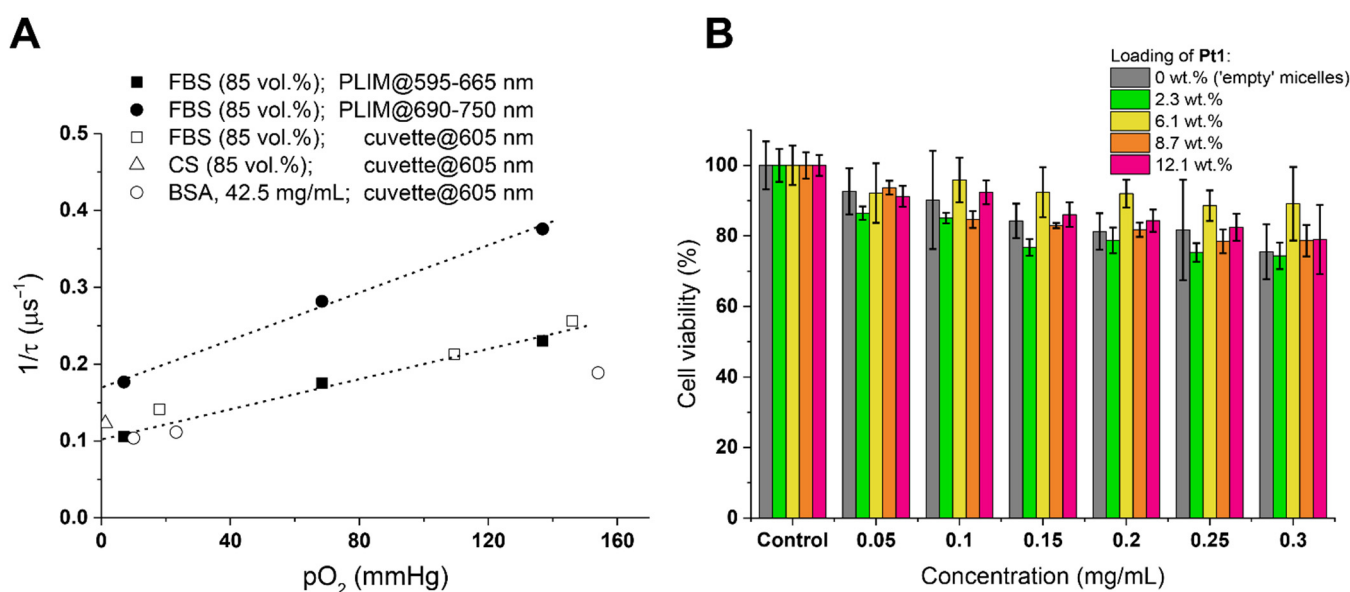


**Figure 4.** (A). Stern–Volmer plots of Pt1@PCL-*b*-PEG (12.1 wt.% of Pt1) in FBS (85 vol.%) measured by PLIM at 37 °C. Excitation at 405 nm. Detection at 595–665 nm and 690–750 nm. Lifetimes measured on lifetime measurement setup (excitation at 355 nm; detection at 605 nm) for FBS (85 vol.%), calf serum (85 vol.%), and BSA (42.5 mg/mL) at 37.7 °C are presented as open symbols for comparison. (B). MTT tests on CHO-K1 cells treated by ‘empty’ PCL-*b*-PEG and ‘loaded’ Pt1@PCL-*b*-PEG micelles (2.3 to 12.1 wt.% of Pt1) for 24 h at 37 °C.

### 3.3. In Vitro Investigation of Pt1@PCL-*b*-PEG Oxygen Probes Inside CHO-K1 Cells

Pt1@PCL-*b*-PEG micellar dispersions of various compositions were first evaluated for their toxicity towards the CHO-K1 cell line by performing an MTT assay. The phosphorescent micelles displayed only slight cytotoxicity that was comparable to that of ‘empty’ PCL-*b*-PEG micelles; in all cases, the cell viability was more than 80% for up to concentrations of 0.3 mg/mL (Figure 4B).

Further, we assessed the phosphorescence lifetimes of Pt1@PCL-*b*-PEG (12.1 wt.%) micellar dispersions in the CHO-K1 cell line under normoxic and hypoxic conditions by phosphorescence lifetime microscopy (PLIM) combined with conventional confocal

microscopy (Figure 5). Analogously to Stern–Volmer plots, PLIM data were recorded using the same two acquisition channels. The living CHO-K1 cells were incubated with probe concentrations of 0.3 mg/mL for 24 h (cell viability at these conditions is more than 80%). Confocal microphotographs revealed complicated intracellular distribution including at least the following two major patterns: diffuse staining of the cytosol and dot-like inclusions (Figure 5A, left column). The same sample areas were then scanned in the PLIM mode to provide the lifetime maps shown in Figure 5A, middle and right columns. Lifetimes of the probe were within the interval from 3.5 to 6  $\mu$ s in the case of normoxia with an average value of 4.0  $\mu$ s, and from 6 to 10  $\mu$ s in hypoxia with an average value of 7–8  $\mu$ s (Figure 5B). The lifetime distributions in both cases are rather wide, demonstrating broad lifetime variations across the same sample.

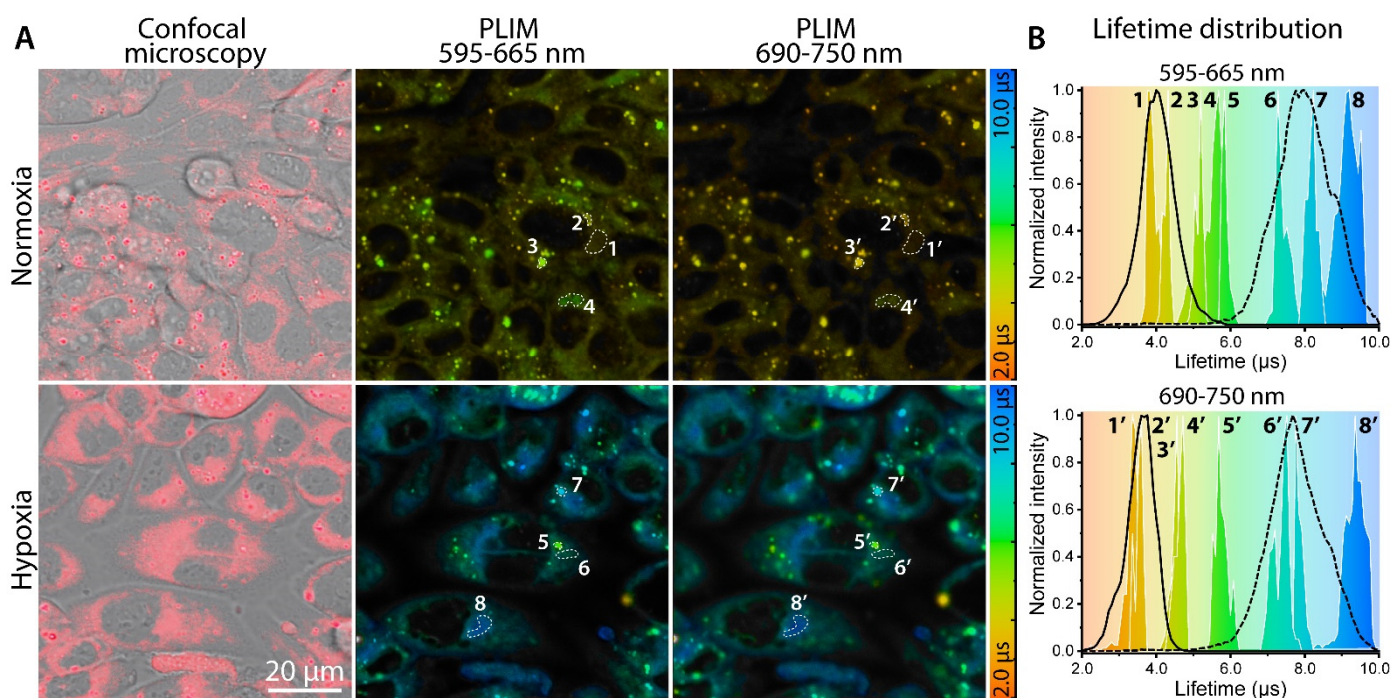


**Figure 5.** (A). Confocal/DIC (left column) and PLIM (middle and right columns) microphotographs of CHO-K1 cells incubated with 0.3 mg/mL Pt1@PCL-*b*-PEG (12.1 wt.% Pt1) for 24 h under normoxic (top row) and hypoxic (bottom row) conditions at 37 °C. Numbers denote selected areas in red (1–8) and deep-red (1’–8’) channels (B). Lifetime distributions of the selected areas (1–8 and 1’–8’) recorded in red channel (595–665 nm; top panel) and deep-red channel (690–750 nm; bottom panel) overlaid with the lifetime distributions across the image for normoxia (solid lines, 2–5  $\mu$ s) and hypoxia (dashed lines, 6–10  $\mu$ s). Excitation: 405 nm; Detection: 663–738 nm (confocal microscopy; left column); 595–665 nm (PLIM; middle column); 690–750 nm (PLIM; right column). Scale bar: 20  $\mu$ m.

Finally, investigation of the influence of incubation period (30 min, 2, 5, and 24 h) on the phosphorescence lifetimes of Pt1@PCL-*b*-PEG (12.1 wt.%) micellar dispersions was performed on the same CHO-K1 cell line under normoxic conditions by PLIM combined with conventional confocal microscopy (Figure 6). Confocal microscopy revealed that the probe’s signal became strong enough to perform PLIM even after 30 min incubation. PLIM data demonstrated a detectable shift in the ‘averaged’ lifetime (i.e., value averaged from lifetime distributions across the image) following the increase in incubation time from 3 to 4  $\mu$ s at 30 min and at 24 h incubation, respectively.

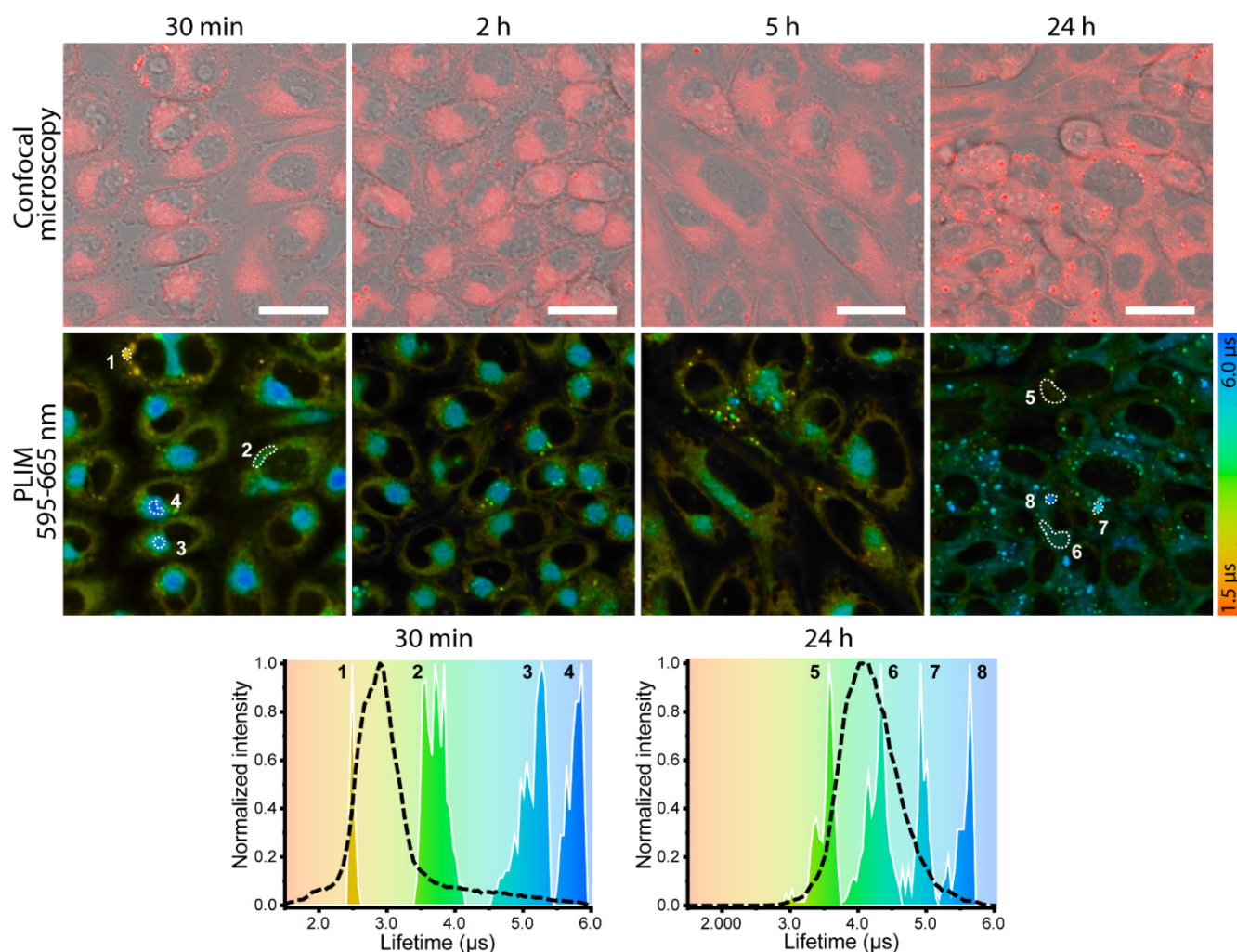


**Figure 6.** Confocal/DIC (top row) and PLIM (middle row) microphotographs of HCO-K1 cells incubated with 0.3 mg/mL Pt1@PCL-*b*-PEG (12.1 wt.% Pt1) for 30 min, 2, 5, and 24 h under normoxia at 37 °C. Bottom row: lifetime distributions of the selected areas (1–8) after 30 min (left) and 24 h (right) incubation overlaid with the lifetime distributions across the image (black dashed lines). Excitation: 405 nm; Detection: 663–738 nm (confocal microscopy, top row); 595–665 nm (PLIM; middle row). Scale bar: 20 μm.

#### 4. Discussion

The present work reported on the aggregation-induced ignition of NIR phosphorescence in Pt1@PCL-*b*-PEG micelles loaded with the non-symmetric platinum (II) complex Pt1 (Scheme 1), which was recently reported by our group [29], together with the evaluation of this system as an intracellular phosphorescent oxygen probe. The micelles were prepared in a similar way to that described in our previous work [31] with slight modifications intended to suppress the precipitation of Pt1 in the course of micelle formation. The non-emissive ‘empty’ PCL-*b*-PEG micelles were also prepared as the ‘control’ system that does not contain the platinum emitter.

The composition of micelles was found to be close to that of the starting reaction mixture (Figure 1B) though it was slightly lower than can be explained by the residual precipitation of Pt1 even under optimized conditions. Nevertheless, the proposed preparation protocol facilitates the loading of PCL-*b*-PEG micelles by Pt1 up to at least 12 wt.% which is in good agreement with our recent report on the high loading capacity of these micelles towards similar organometallic complexes [31]. The ‘loaded’ micelles revealed almost unimodal size distributions (Figure 1A) with the average hydrodynamic radius

( $R_h$ ) of **Pt1@PCL-*b*-PEG**, which did not exceed 19 nm for all the compositions studied and is close to the value obtained for the ‘empty’ micelles (22 nm) as well as to that reported earlier (17.7 nm [31]). Intensity weighted  $R_h$  distributions also indicated a non-negligible contribution from larger particles, with an  $R_h$  of ca. 80–200 nm, which presumably represent aggregates of micelles [31]). However, our previous evaluation of weight fractions of aggregates in similar phosphorescent micelles demonstrated that the comparable contribution of larger particles into light scattering is a result of substantially higher sensitivity of light scattering to the particle size and corresponds to trace amounts of aggregates [31]. Due to their small sizes, the resulting phosphorescent micelles appeared to be quite stable towards precipitation (*vide supra*, Section 3.1.) not only in water but also in PBS, and this behavior was superior compared to conventional polymer nanoparticles stabilized by electrostatic repulsion [28]. Consequently, the obtained **Pt1@PCL-*b*-PEG** polymer nanoparticles look very promising as biocompatible carriers for luminescent emitters.

The major photophysical effect observed for **PCL-*b*-PEG** micelles loaded with the mononuclear platinum emitters consists of the ignition of NIR luminescence. Figure 2C and Figure S4 demonstrate emergence and stepwise growth of a broad luminescence band centered at ca. 790 nm with the increase in **Pt1** content in the micelles from 1.8 to 12.1 wt.% accompanied by a 3-fold increase in quantum yield values (from 2% for 2.5 wt.% of **Pt1** loading to 6% for 12.4 wt.% of **Pt1** loading). Similar effects were observed earlier for the analogous system (symmetric [Pt (C<sup>N</sup>\*N<sup>C</sup>)] complex embedded into aminated polystyrene nanoparticles [5]) but in that case only deep-red emission was achieved. Based on the recent literature data [5,17–20] it is possible to assign the observed NIR luminescence to aggregation-induced emission. The aggregation of monomeric **Pt1** molecules in the micelles core is evidently the most natural process for the hydrophobic platinum complex in a hydrophilic media that was previously found in closely analogous systems, e.g., in the mixed (NCMe-H<sub>2</sub>O and THF-H<sub>2</sub>O) solvents [19,29], containing water and hydrophobic organic components. The NIR band profiles obtained by deconvolution of experimental emission spectra are nearly identical for all micelles compositions from 1.8 to 12.1 wt.% (Figure 2D) that points to the essentially similar nature of NIR emissive chromophores independent of the **Pt1** content in the micelles. The spectra of the obtained species differed only in the relative emission intensity from monomeric complexes and aggregated emitters that is a result of the concentration driven equilibria of the aggregates formation from mononuclear complexes  $n^*\text{Pt1} \leftrightarrow [\text{Pt1}]_n$ . It was found earlier that even the formation of dimers ( $2^*\text{Pt1} \leftrightarrow [\text{Pt1}]_2$ ) with short Pt . . . Pt contacts completely changes the character of the emissive excited state. The dimers with metallophilic bonding either in the ground or in excited state are responsible for the red shift of emission compared to the starting chromophore and crucial changes in the character of emissive excited states [19,29]. It is worth noting that, contrary to the emission spectra, the excitation and normalized absorption spectra are almost independent of the extent of **Pt1** loading and the detection wavelength (Figure 2A,B and Figure S3). These findings indicate that the observed NIR emission most probably occurs from the excimer with a metal–metal-to-ligand charge-transfer (<sup>3</sup>MMLCT) character [34,35] rather than from the ground-state of the dimers or oligomers with the Pt . . . Pt bonding [5].

Time-resolved photophysical studies of the **Pt1@PCL-*b*-PEG** micelles with the lowest (2.3 wt.% of **Pt1**; Figure S7) and highest (12.1 wt.% of **Pt1**; Figure S8) emitter loadings were performed at the detection wavelength of 605 nm as the monomolecular and aggregated chromophores displayed a substantial contribution in the emission decay at this wavelength. This choice looks natural for the probe with a low **Pt1** content, where the observed emission was mainly determined by the monomolecular chromophore. Unfortunately, the TCSPC detector sensitivity at 780 nm was too weak to obtain reliable photon counting statistics for both types of species at this wavelength. However, the measurements for the probes with 12.1 wt.% of **Pt1** at intermediate wavelengths (665 and 725 nm), *vide supra* (Results Section), for which the detector sensitivity was acceptable, revealed that even in the case of biexponential fitting, the contributions of the major decay component was 92–95% with the

lifetime values independent of the detection wavelength (Table S2). Taking into account these observations, we can conclude that the decays obtained at 605 nm for water and PBS dispersions were monoexponential, and the minor components can be neglected without a loss of valuable information. Thus, the resulting decay curves were satisfactorily fitted using the monoexponential function in the case of aqueous solutions (water, PBS) but the triple exponential treatment was necessary to fit the decay curves in the media containing biomacromolecules, e.g., bovine serum albumin (BSA) (Figures S7 and S8). Triexponential fitting was chosen because of the substantial non-monoexponential character of the corresponding decay curves (Figures S7 and S8) that could not fit by biexponential fitting in most cases. The physical rationale of such a sophisticated treatment lies in our hypothesis regarding the non-negligible interaction of **Pt1@PCL-*b*-PEG** with the serum components, predominantly, with BSA, *vide infra*.

The lifetimes of **Pt1@PCL-*b*-PEG** in water and PBS demonstrated substantial dependence on the partial pressure of oxygen (Figure 3B; Table 1). The ratio of lifetimes in degassed and aerated dispersions ( $\tau_0/\tau_{160}$ ) varied from 1.5 in the case of 12.1 wt.% of **Pt1** to 3.0 in the case of 2.3 wt.% of **Pt1**. Stern–Volmer plots of **Pt1@PCL-*b*-PEG** (2.3 to 12.1 wt.%) luminescence recorded in aqueous dispersions (in both water and PBS) revealed the linear dependence of reciprocal lifetime on the partial pressure of molecular oxygen in solution and insensitivity of the sensory response towards the presence of low-molecular electrolytes (PBS vs. water), Figure 3A. The absolute values of lifetimes display rather pronounced dependence on the extent of **Pt1** loading, which is evidently related to transformation of emissive centers upon an increase in the **Pt1** content in the micelles, from predominantly mononuclear emitters to the aggregates with Pt . . . Pt bonding. At higher (>9 wt.%) **Pt1** loadings (Figure 3B), the lifetime stay nearly constant which indicates a major contribution from the aggregated emitters. Moreover, the combination of the independence of lifetime values as well as their sensitivities to oxygen at high **Pt1** (>9 wt.%) loadings with the independence of lifetime from detection wavelength at 12.1 wt.% **Pt1** loading for the case of 12.1 wt.% of **Pt1** suggests that, at least at this composition, the resulting phosphorescent micelles demonstrate preferential emission from aggregates at all detection wavelengths (including that of 605 nm). This situation becomes even more pronounced in aerated media, since under these conditions the emission of non-aggregated **Pt1** is strongly quenched due to higher sensitivity to oxygen. In this context, it is reasonable to focus on 12.1 wt.% **Pt1** loading during the evaluation of **Pt1@PCL-*b*-PEG** as an oxygen sensor (the last part of the study).

To elucidate lifetime cross-sensitivity to various biasing parameters, we measured the lifetimes of **Pt1@PCL-*b*-PEG** in aerated PBS at different pH ranging from 5.8 to 8.1, at different sensor concentrations (0.2 vs. 0.4 mg/mL) and two temperatures (25.6 °C vs. 37.6 °C) as well as in the presence of reactive oxygen species (100 nm H<sub>2</sub>O<sub>2</sub>, the upper limit of physiologically relevant H<sub>2</sub>O<sub>2</sub> content) and BSA. The results summarized in Table 2 demonstrate that temperature and the presence of BSA are two microenvironmental parameters that, in addition to the extent of **Pt1** loading, substantially affect lifetime characteristics. The temperature effect is very well known, is not unexpected and can be corrected by performing calibrations and PLIM experiments at the same temperature. Using more complicated biological fluids such as FBS or calf serum results in even more complex decay curves (Figure S8) that can be fit by triexponential fitting, *vide supra*. The resulting mean lifetimes (Table S3) were substantially higher compared to those measured in water or PBS, as well as in 0.25 mg/mL BSA (Table 2). One can assume that the major component affecting lifetimes in these media are proteins (predominantly, BSA), and this hypothesis is supported by deep analogies in both emission spectra (Figure S9) and lifetimes (Table S3) observed in BSA solutions of a high concentration (42.5 mg/mL) which is equivalent to this protein content in the 85 vol.% serum used in the present study.

Such an unexpected behavior of phosphorescent micelles in serum can be explained by the influence of serum proteins, especially albumin, on the integrity of the micelles. Indeed, BSA is a transport protein featuring high solubilization efficiency towards hydrophobic

molecules [36]. At relatively low protein concentrations, the micelles rather effectively protect Pt1 from interactions with proteins; however, at extremely high protein concentrations, it seems that BSA can compete with micelles for binding with Pt1 and solubilize part of this complex by the formation of non-covalent adducts [37–39]. This can result in the appearance of a new form of the emitter (non-covalent adducts Pt1-BSA) featuring its own decay profile. Such an interaction further complicates the lifetime decay profile leading to the necessity of multiexponential fitting specific for serum and BSA solutions (Figure S8, Table S3). The hypothesis of the dominant impact of BSA on lifetimes of phosphorescent micelles is corroborated by the fact that in BSA solutions of a high concentration (42.5 mg/mL) the spectral profile (Figure S9) and lifetime (Table S3) changes are almost the same as in the FBS.

The major practically important consequence of the above findings is that the application of the sensor systems of this type in quantitative O<sub>2</sub> sensing requires obtaining the calibration curves at a fixed temperature (equal to that intended for further sensing experiments) and in the model media with the composition as close as possible to that of cell cytosol. Recently, we found that FBS is a relevant model media mimicking intracellular environment [22]. Hence, we performed the calibration of Pt1@PCL-*b*-PEG (12.1 wt.%) in FBS at 37 °C at 0.3 mg/mL of the probe (Figure 4A) using the PLIM instrument. The resulting Stern–Volmer plot is linear (Figure 4A), and the absolute lifetime values are close to those measured in cuvette in FBS and 42.5 mg/mL BSA (Figure 4A).

MTT tests showed that the Pt1@PCL-*b*-PEG probe is not cytotoxic towards CHO-K1 cells if incubated for 24 h at concentrations of up to 0.3 mg/mL (Figure 4B). We thus evaluated the oxygen sensing performance of the Pt1@PCL-*b*-PEG probe at this concentration and incubation time by carrying out PLIM on CHO-K1 cells under the conditions of normoxia and hypoxia. The PLIM results demonstrate significant lifetime sensitivity of the Pt1@PCL-*b*-PEG probe towards O<sub>2</sub> partial pressure comparable to other NIR O<sub>2</sub> probes [22] in both red (595–665 nm) and NIR (690–750) channels (Figure 5). This level of sensitivity allows for the unambiguous detection of the oxygenation state of cells and differentiation of hypoxia vs. normoxia (the same result was achieved for lower Pt1 loadings, see Figure S10). Moreover, the range of lifetimes variation fits well with the region observed in the Stern–Volmer plots that provides at least semi-quantitative evaluation of O<sub>2</sub> partial pressures from PLIM data.

It is worth noting that Pt1@PCL-*b*-PEG rapidly accumulates inside the cells and distributes throughout the cytoplasm, and 30 min incubation is sufficient to obtain luminescence signal strong enough to run PLIM experiment (Figure 6). Dependence of ‘averaged’ lifetime (i.e., the value averaged from the lifetime distributions across the image) on incubation time demonstrates the progressive increase in this parameter during the incubation. The observed increase in lifetime upon increasing the incubation time could be the result of (at least a partial) interaction of Pt1@PCL-*b*-PEG with serum proteins that was shown to result in a lifetime increase, *vide supra*. Alternatively, the observed effect can correlate with the observed accumulation of dot-like inclusions inside cells that significantly contribute to the overall phosphorescence signal after 24 h incubation (Figure 6). Obviously, the unambiguous interpretation of the observed effect requires a much deeper evaluation of the intracellular fate of the Pt1@PCL-*b*-PEG probe and is well beyond the scope of the present study.

## 5. Conclusions

In conclusion, the present work described the first example of the preparation of biocompatible NIR emitters by using the effect of nanoconfined AIE generation from the non-symmetric [Pt (C<sup>N</sup>\*N<sup>ˆ</sup>C<sup>ˆ</sup>)] complex in block copolymer micelles (PCL-*b*-PEG). The observed aggregation-induced NIR phosphorescence becomes more prominent at increased Pt1 loading into the micelles and features a high two-photon absorption cross-section (450 GM). Both effects are believed to be the result of progressive Pt1 aggregation inside the hydrophobic cores of the PCL-*b*-PEG micelles. Compared to the closest liter-

ature analog (symmetric [Pt (C<sup>^</sup>N\*N<sup>^</sup>C)] complex embedded into aminated polystyrene nanoparticles [5]), the present Pt1@PCL-*b*-PEG O<sub>2</sub> nanoprobe demonstrated improved stability in aqueous physiological dispersions combined with bright NIR phosphorescence retaining pronounced sensitivity towards molecular oxygen. The detailed time-resolved photophysical analysis of NIR phosphorescence in nanosecond interval revealed that NIR emission results from the excimeric excited state of the <sup>3</sup>MMLCT character. Evaluation of the Pt1@PCL-*b*-PEG efficacy as a lifetime intracellular oxygen biosensor showed that the probe displays a linear response of the emission lifetime onto variations in the concentration of oxygen which, however, is compromised by a pronounced influence of protein components of the physiological media. Therefore, Pt1@PCL-*b*-PEG can serve only as a semi-quantitative lifetime O<sub>2</sub> nanosensor. Nevertheless, the present study proved the applicability of an alternative approach for creating NIR O<sub>2</sub> biosensors that avoids the sophisticated synthesis of NIR emitters by using the aggregation-induced ignition of NIR phosphorescence instead. Further improvement of the present sensor prototype can be achieved by the enhancement of its insensitivity to serum components, for example, by cross-linking the micelles.

**Supplementary Materials:** The following supporting information can be downloaded at: <https://www.mdpi.com/article/10.3390/bios12090695/s1> as a single pdf file: Table S1: Characterization of PCL-*b*-PEG samples compositions by <sup>1</sup>H NMR and GPC; Figure S1: <sup>1</sup>H NMR spectra of PCL-*b*-PEG samples; Figure S2: Calibration curve of Pt1 absorption in DMF at 381 nm in the presence of 0.25 mg/mL of PCL-*b*-PEG; Figure S3: Normalized excitation spectra of Pt1@PCL-*b*-PEG; Figure S4: Non-normalized emission spectra of Pt1@PCL-*b*-PEG; Figure S5: The emission rise and decay kinetics of Pt1@PCL-*b*-PEG; Figure S6: The Z-scan profiles of Pt1 and Pt1@PCL-*b*-PEG; Figures S7 and S8: Luminescence decay curves of Pt1@PCL-*b*-PEG in aerated dispersions. Tables S2 and S3: Summary of lifetime characteristics of Pt1@PCL-*b*-PEG; Figure S9: Luminescence spectra of Pt1@PCL-*b*-PEG in different media. Figure S10: PLIM microphotographs of CHO-K1 cells stained by Pt1@PCL-*b*-PEG of various Pt1 loadings.

**Author Contributions:** Conceptualization, P.-T.C., P.S.C. and S.P.T.; methodology, N.A.Z., A.I.S. and Y.-C.L.; validation, N.A.Z., A.I.S. and Y.-C.L.; formal analysis, N.A.Z., A.I.S., Y.-C.L. and P.S.C.; investigation, N.A.Z., A.I.S. and Y.-C.L.; resources, E.E.G. and A.F.K.; data curation, N.A.Z., A.I.S., Y.-C.L. and P.S.C.; writing—original draft preparation, N.A.Z., Y.-C.L. and P.S.C.; writing—review and editing, A.I.S., E.E.G., A.F.K., P.-T.C., P.S.C. and S.P.T.; visualization, A.I.S.; supervision, P.-T.C. and S.P.T.; project administration, P.-T.C. and P.S.C.; funding acquisition, P.-T.C. and P.S.C. All authors have read and agreed to the published version of the manuscript.

**Funding:** The reported study was funded by RFBR and MOST according to the joint research project № 20-53-S52001.

**Institutional Review Board Statement:** Not applicable.

**Informed Consent Statement:** Not applicable.

**Acknowledgments:** The experimental studies were carried out using equipment of the Research Park of St. Petersburg State University (Centres for Magnetic Resonance, for Optical and Laser Materials Research, for Chemical Analysis and Materials Research, and for Diagnostics of Functional Materials for Medicine, Pharmacology and Nanoelectronics). We also thank Petr S. Vlasov for running the GPC experiments.

**Conflicts of Interest:** The authors declare no conflict of interest.

## References

1. Luo, J.; Xie, Z.; Lam, J.W.Y.; Cheng, L.; Tang, B.Z.; Chen, H.; Qiu, C.; Kwok, H.S.; Zhan, X.; Liu, Y.; et al. Aggregation-Induced Emission of 1-Methyl-1,2,3,4,5-Pentaphenylsilole. *Chem. Commun.* **2001**, *18*, 1740–1741. [[CrossRef](#)] [[PubMed](#)]
2. Hong, Y.; Lam, J.W.Y.; Tang, B.Z. Aggregation-Induced Emission. *Chem. Soc. Rev.* **2011**, *40*, 5361–5388. [[CrossRef](#)]
3. Mei, J.; Hong, Y.; Lam, J.W.Y.; Qin, A.; Tang, Y.; Tang, B.Z. Aggregation-Induced Emission: The Whole Is More Brilliant than the Parts. *Adv. Mater.* **2014**, *26*, 5429–5479. [[CrossRef](#)] [[PubMed](#)]
4. Mei, J.; Leung, N.L.C.; Kwok, R.T.K.; Lam, J.W.Y.; Tang, B.Z. Aggregation-Induced Emission: Together We Shine, United We Soar! *Chem. Rev.* **2015**, *115*, 11718–11940. [[CrossRef](#)] [[PubMed](#)]



5. Maisuls, I.; Wang, C.; Gutierrez Suburu, M.E.; Wilde, S.; Daniliuc, C.-G.; Brünink, D.; Doltsinis, N.L.; Ostendorp, S.; Wilde, G.; Kösters, J.; et al. Ligand-Controlled and Nanoconfinement-Boosted Luminescence Employing Pt (ii) and Pd (ii) Complexes: From Color-Tunable Aggregation-Enhanced Dual Emitters towards Self-Referenced Oxygen Reporters. *Chem. Sci.* **2021**, *12*, 3270–3281. [[CrossRef](#)] [[PubMed](#)]
6. Gao, X.; Sun, J.Z.; Tang, B.Z. Reaction-Based AIE-Active Fluorescent Probes for Selective Detection and Imaging. *Isr. J. Chem.* **2018**, *58*, 845–859. [[CrossRef](#)]
7. Yu, H.; Chen, B.; Huang, H.; He, Z.; Sun, J.; Wang, G.; Gu, X.; Tang, B.Z. AIE-Active Photosensitizers: Manipulation of Reactive Oxygen Species Generation and Applications in Photodynamic Therapy. *Biosensors* **2022**, *12*, 348. [[CrossRef](#)] [[PubMed](#)]
8. Qi, C.; Wang, X.; Chen, Z.; Xiang, S.; Wang, T.; Feng, H.T.; Tang, B.Z. Organometallic AIEgens for Biological Theranostics. *Mater. Chem. Front.* **2021**, *5*, 3281–3297. [[CrossRef](#)]
9. Liu, J.; Jin, C.; Yuan, B.; Liu, X.; Chen, Y.; Ji, L.; Chao, H. Selectively Lighting up Two-Photon Photodynamic Activity in Mitochondria with AIE-Active Iridium (iii) Complexes. *Chem. Commun.* **2017**, *53*, 2052–2055. [[CrossRef](#)]
10. Qiu, K.; Ouyang, M.; Liu, Y.; Huang, H.; Liu, C.; Chen, Y.; Ji, L.; Chao, H. Two-Photon Photodynamic Ablation of Tumor Cells by Mitochondria-Targeted Iridium (iii) Complexes in Aggregate States. *J. Mater. Chem. B* **2017**, *5*, 5488–5498. [[CrossRef](#)]
11. Sheet, S.K.; Sen, B.; Patra, S.K.; Rabha, M.; Aguan, K.; Khatua, S. Aggregation-Induced Emission-Active Ruthenium(II) Complex of 4,7-Dichloro Phenanthroline for Selective Luminescent Detection and Ribosomal RNA Imaging. *ACS Appl. Mater. Interfaces* **2018**, *10*, 14356–14366. [[CrossRef](#)] [[PubMed](#)]
12. Sen, B.; Patra, S.K.; Khatua, S. Ruthenium (II) Polypyridine Complex-Based Aggregation-Induced Emission Luminogen for Rapid and Selective Detection of Phosgene in Solution and in the Gas Phase. *Inorg. Chem.* **2021**, *60*, 19175–19188. [[CrossRef](#)] [[PubMed](#)]
13. Sathish, V.; Ramdass, A.; Lu, Z.-Z.; Velayudham, M.; Thanasekaran, P.; Lu, K.-L.; Rajagopal, S. Aggregation-Induced Emission Enhancement in Alkoxy-Bridged Binuclear Rhenium (I) Complexes: Application as Sensor for Explosives and Interaction with Microheterogeneous Media. *J. Phys. Chem. B* **2013**, *117*, 14358–14366. [[CrossRef](#)]
14. Liu, H.-Q.; Peng, Y.-X.; Zhang, Y.; Yang, X.-Q.; Feng, F.-D.; Luo, X.-B.; Yan, L.-S.; Hu, B.; Huang, W. Aggregation-Induced Emission Generation via Simultaneous N-Alkylation and rhenium (I) Tricarbonyl Complexation for 2-(2-thienyl)imidazo[4,5-f][1,10]-Phenanthroline. *Dye. Pigment.* **2020**, *174*, 108074. [[CrossRef](#)]
15. Gabr, M.T.; Pigge, F.C. Rhenium Tricarbonyl Complexes of AIE Active Tetraarylethylene Ligands: Tuning Luminescence Properties and HSA-Specific Binding. *Dalt. Trans.* **2017**, *46*, 15040–15047. [[CrossRef](#)] [[PubMed](#)]
16. Zhang, J.; Zou, H.; Wang, X.; He, B.; Liu, S.H.; Lam, J.W.Y.; Tang, B.Z. New AIE-Active Copolymers with Au(I) Isocyanide Acrylate Units. *J. Inorg. Organomet. Polym. Mater.* **2020**, *30*, 1490–1496. [[CrossRef](#)]
17. Cuerva, C.; Campo, J.A.; Cano, M.; Lodeiro, C. Multi-Stimuli-Responsive Properties of Aggregation-Enhanced Emission-Active Unsymmetrical Pt II Metallomesogens through Self-Assembly. *Chem.–A Eur. J.* **2019**, *25*, 12046–12051. [[CrossRef](#)]
18. Martínez-Junquera, M.; Lalinde, E.; Moreno, M.T.; Alfaro-Arnedo, E.; López, I.P.; Larráyo, I.M.; Pichel, J.G. Luminescent Cyclometalated Platinum (ii) Complexes with Acyclic Diaminocarbene Ligands: Structural, Photophysical and Biological Properties. *Dalt. Trans.* **2021**, *50*, 4539–4554. [[CrossRef](#)]
19. Gong, Z.-L.; Tang, K.; Zhong, Y.-W. A Carbazole-Bridged Biscyclometalated Diplatinum Complex: Synthesis, Characterization, and Dual-Mode Aggregation-Enhanced Phosphorescence. *Inorg. Chem.* **2021**, *60*, 6607–6615. [[CrossRef](#)]
20. Yang, J.; Sun, L.; Hao, L.; Yang, G.-G.; Zou, Z.-C.; Cao, Q.; Ji, L.-N.; Mao, Z.-W. A Halogen Ion-Selective Phosphorescence Turn-on Probe Based on Induction of Pt–Pt Interactions. *Chem. Commun.* **2019**, *55*, 11191–11194. [[CrossRef](#)]
21. Kritchenkov, I.S.; Elistratova, A.A.; Sokolov, V.V.; Chelushkin, P.S.; Shirmanova, M.V.; Lukina, M.M.; Dudenkova, V.V.; Shcheslavskiy, V.I.; Kalinina, S.; Reef, K.; et al. A Biocompatible Phosphorescent Ir (iii) Oxygen Sensor Functionalized with Oligo (ethylene Glycol) Groups: Synthesis, Photophysics and Application in PLIM Experiments. *New J. Chem.* **2020**, *44*, 10459–10471. [[CrossRef](#)]
22. Kritchenkov, I.S.; Solomatina, A.I.; Kozina, D.O.; Porsev, V.V.; Sokolov, V.V.; Shirmanova, M.V.; Lukina, M.M.; Komarova, A.D.; Shcheslavskiy, V.I.; Belyaeva, T.N.; et al. Biocompatible Ir (III) Complexes as Oxygen Sensors for Phosphorescence Lifetime Imaging. *Molecules* **2021**, *26*, 2898. [[CrossRef](#)] [[PubMed](#)]
23. Esipova, T.V.; Barrett, M.J.P.; Erlebach, E.; Masunov, A.E.; Weber, B.; Vinogradov, S.A. Oxyphor 2P: A High-Performance Probe for Deep-Tissue Longitudinal Oxygen Imaging. *Cell Metab.* **2019**, *29*, 736–744. [[CrossRef](#)]
24. Tsytsarev, V.; Arakawa, H.; Borisov, S.; Pumbo, E.; Erzurumlu, R.S.; Papkovsky, D.B. In Vivo Imaging of Brain Metabolism Activity Using a Phosphorescent Oxygen-Sensitive Probe. *J. Neurosci. Methods* **2013**, *216*, 146–151. [[CrossRef](#)]
25. Chien, J.S.; Mohammed, M.; Eldik, H.; Ibrahim, M.M.; Martinez, J.; Nichols, S.P.; Wisniewski, N.; Klitzman, B. Injectable Phosphorescence-Based Oxygen Biosensors Identify Post Ischemic Reactive Hyperoxia. *Sci. Rep.* **2017**, *7*, 8255. [[CrossRef](#)]
26. Rivera, K.R.; Pozdin, V.A.; Young, A.T.; Erb, P.D.; Wisniewski, N.A.; Magness, S.T.; Daniele, M. Integrated Phosphorescence-Based Photonic Biosensor (iPOB) for Monitoring Oxygen Levels in 3D Cell Culture Systems. *Biosens. Bioelectron.* **2019**, *123*, 131–140. [[CrossRef](#)] [[PubMed](#)]
27. Chelushkin, P.S.; Shkirova, J.R.; Kritchenkov, I.S.; Baigildin, V.A.; Tunik, S.P. Phosphorescent NIR Emitters for Biomedicine: Applications, Advances and Challenges. *Dalt. Trans.* **2022**, *51*, 1257–1280. [[CrossRef](#)]
28. Borisov, S.M.; Mayr, T.; Mistberger, G.; Waich, K.; Koren, K.; Chojnacki, P.; Klimant, I. Precipitation as a Simple and Versatile Method for Preparation of Optical Nanochemosensors. *Talanta* **2009**, *79*, 1322–1330. [[CrossRef](#)] [[PubMed](#)]

29. Solomatina, A.I.; Galenko, E.E.; Kozina, D.O.; Kalinichev, A.A.; Baigildin, V.A.; Prudovskaya, N.A.; Shakirova, J.R.; Khlebnikov, A.F.; Porsev, V.V.; Evarestov, R.A.; et al. Non-Symmetric [Pt(C<sup>^</sup>N\*N<sup>^</sup>C<sup>^</sup>)] Complexes: Aggregation Induced Emission in Solid State and in Nanoparticles Tuned by Ligand Structure. *Chem. Eur. J.* 2022; submitted.
30. Weissleder, R.A. Clearer Vision for in vivo Imaging. *Nat. Biotechnol.* **2001**, *19*, 316–317. [[CrossRef](#)]
31. Elistratova, A.A.; Kritchenkov, I.S.; Lezov, A.A.; Gubarev, A.S.; Solomatina, A.I.; Kachkin, D.V.; Shcherbina, N.A.; Liao, Y.-C.; Liu, Y.-C.; Yang, Y.-Y.; et al. Lifetime Oxygen Sensors Based on Block Copolymer Micelles and Non-Covalent Human Serum Albumin Adducts Bearing Phosphorescent Near-Infrared Iridium (III) Complex. *Eur. Polym. J.* **2021**, *159*, 110761. [[CrossRef](#)]
32. Mosmann, T. Rapid Colorimetric Assay for Cellular Growth and Survival: Application to Proliferation and Cytotoxicity Assays. *J. Immunol. Methods* **1983**, *65*, 55–63. [[CrossRef](#)]
33. Conway, J.R.W.; Warren, S.C.; Herrmann, D.; Murphy, K.J.; Cazet, A.S.; Vennin, C.; Shearer, R.F.; Killen, M.J.; Magenau, A.; Méléneq, P.; et al. Intravital Imaging to Monitor Therapeutic Response in Moving Hypoxic Regions Resistant to PI3K Pathway Targeting in Pancreatic Cancer. *Cell Rep.* **2018**, *23*, 3312–3326. [[CrossRef](#)] [[PubMed](#)]
34. Vezzu, D.A.K.; Deaton, J.C.; Jones, J.S.; Bartolotti, L.; Harris, C.F.; Marchetti, A.P.; Kondakova, M.; Pike, R.D.; Huo, S. Highly Luminescent Tetradentate Bis-Cyclometalated Platinum Complexes: Design, Synthesis, Structure, Photophysics, and Electroluminescence Application. *Inorg. Chem.* **2010**, *49*, 5107–5119. [[CrossRef](#)]
35. Wilde, S.; González-Abradelo, D.; Daniliuc, C.-G.; Böckmann, M.; Doltsinis, N.L.; Strassert, C.A. Fluorination-Controlled Aggregation and Intermolecular Interactions in Pt (II) Complexes with Tetradentate Luminophores. *Isr. J. Chem.* **2018**, *58*, 932–943. [[CrossRef](#)]
36. Fasano, M.; Curry, S.; Terreno, E.; Galliano, M.; Fanali, G.; Narciso, P.; Notari, S.; Ascenzi, P. The Extraordinary Ligand Binding Properties of Human Serum Albumin. *IUBMB Life (Int. Union Biochem. Mol. Biol. Life)* **2005**, *57*, 787–796. [[CrossRef](#)]
37. Chelushkin, P.S.; Krupenya, D.V.; Tseng, Y.-J.; Kuo, T.-Y.; Chou, P.-T.; Koshevoy, I.O.; Burov, S.V.; Tunik, S.P. Water-Soluble Noncovalent Adducts of the Heterometallic Copper Subgroup Complexes and Human Serum Albumin with Remarkable Luminescent Properties. *Chem. Commun.* **2014**, *50*, 849–851. [[CrossRef](#)]
38. Solomatina, A.I.; Baigildin, V.A.; Zhukovsky, D.D.; Krupenya, D.V.; Koshel, E.I.; Shcheslavskiy, V.I.; Tunik, S.P.; Chelushkin, P.S. How to Avoid Protein Aggregation to Improve Cellular Uptake of Albumin-Based Conjugates: Towards the Rational Design of Cell-Penetrable Phosphorescent Probes. *Colloid Polym. Sci.* **2019**, *297*, 325–337. [[CrossRef](#)]
39. Kritchenkov, I.S.; Chelushkin, P.S.; Sokolov, V.V.; Pavlovskiy, V.V.; Porsev, V.V.; Evarestov, R.A.; Tunik, S.P. Near-Infrared [Ir(N<sup>^</sup>C)<sub>2</sub>(N<sup>^</sup>N)] + Emitters and Their Noncovalent Adducts with Human Serum Albumin: Synthesis and Photophysical and Computational Study. *Organometallics* **2019**, *38*, 3740–3751. [[CrossRef](#)]